# Highly degenerate photonic flat bands arising from complete graph configurations

Hanyu Wang,[1] Biao Yang,[1,2,*] Wei Xu,[1] Yuancheng Fan,[2] Qinghua Guo,[2] Zhihong Zhu,[1,†] and C. T. Chan[2,‡]
[1] *College of Advanced Interdisciplinary Studies, National University of Defense Technology, Changsha 410073, China*
[2] *Department of Physics and Center for Metamaterials Research, The Hong Kong University of Science and Technology, Hong Kong, China*

(Received 19 May 2019; revised manuscript received 19 September 2019; published 30 October 2019)

Inspired by complete graph theory, we demonstrate that a metallic claw "meta-atom" structure can carry a high number of nearly degenerate resonant modes. A photonic metacrystal composed of a lattice of such meta-atoms exhibits a large number of flat bands that are squeezed into a narrow frequency window, and these flat bands can be designed to locate in a wide complete three-dimensional band gap. The degeneracy dimension ($N_f$) of the flat bands is determined by the number of branches ($N_b$) of the metallic claw with $N_f = N_b$–3, which is geometrically related to the complete graph theory. Different from those flat bands emerging from special lattice arrangements (e.g., kagome lattice), the isolated flat bands here are insensitive to lattice perturbations. The proposed mechanism offers a platform for realizing various dispersionless phenomena and a paradigm to realize high density of states and spectra compressing.

DOI: 10.1103/PhysRevA.100.043841

## I. INTRODUCTION

Flat bands [1–5] refer to the fact that spectral bands are dispersionless or nearly so and their energy spectrum $E(\vec{k})$ is almost independent of momentum $\vec{k}$. In photonics, the realization of flat bands has been long pursued [6] for enhancing light-matter interaction with slow light [7–9] and wave localization [10,11], or it offers platforms for other applications such as distortion-free imaging and pulse buffering in nonlinear optics [12,13]. Typically, flat bands are found in the Dice [1], Lieb [3], kagome [14,15], and other lattices [16,17] due to destructive interference, where fine-tuned nearest- and next-nearest neighboring hopping parameters are the key factors. Researchers have used waveguide arrays [10,18–23], dielectric-plasmonic resonators [24–32], and fine-tuned photonic crystals [33–35] to realize photonic flat bands, where high dielectric contrast or exact lattice symmetry are required. However, these mechanisms inspired by analogies with "frustrated" condensed matter systems [5,36,37] exhibit many limitations in the photonic regime where photonic bands usually arise from multiple coherent scattering rather than the hopping of local atomic orbits. Moreover, realization of full three-dimensional flat bands [38] is very challenging using such lattice arrangement.

In this paper, we propose the realization of isolated three-dimensional (3D) photonic flat bands, which locate in a wide complete band gap [39,40]. The number of flat bands can be determined by a simple arithmetic formula and can be controllably large. More importantly, this large number of flat bands can be squeezed into a narrow frequency window, leading to an extremely high density of states (DOS). The flat bands emerge from local resonances enabled by connectivity of the metallic claw structure, and can be described by graph theory. As the existence of the flat bands does not depend on crystalline symmetry, they are more robust against imperfections.

Recently, geometric aspects of physics have attracted a lot of attention. In photonics, various topological photonic semimetals and insulators [41] have been theoretically proposed and experimentally verified. Their properties are characterized by integers and are stable against local perturbations. For example, the number of edge states of photonic the Haldane model [42,43] is directly related to its bulk integer Chern number defined in momentum (parameter) space [44].

Here, the real space geometry of the meta-atom generates interesting physics. We will start with the metallic claw structure, then use effective electric circuit theory to explain the underlying connectivity relation between any two branches, and finally find the complete graph configuration [45] and predict the large number of degenerate flat bands.

## II. RESULTS: METALLIC CLAW STRUCTURE AND PHOTONIC FLAT BAND

The metallic claw structure with $C_4$ rotation symmetry is shown in Fig. 1(a). Each meta-atom consists of two perpendicularly placed split ring resonators (SRRs) which touch each other on the top, forming a four-branch claw. The claw metallic structure has length $l = 1.95$ mm, gap $g = 0.615$ mm, and diameter $r = 0.21$ mm as indicated in Fig. 1(a). The whole metacrystal is formed by arranging the claw structure in a simple 3D cubic lattice with lattice constant $a = 3.5$ mm. In the simulation, we assume the hosting material is air and regard metallic components as perfect electric conductors (PECs), which is a good approximation in microwave, terahertz, and even far-infrared bands. Figure 1(b) schematically shows the effective electric circuit describing the underlying connectivity relation of the metallic claw structure [46,47]. We have effectively introduced the capacitance $C'$ (between next-nearest neighbor branches) to distinguish with $C$ arising from those nearest neighbor branches.

*yangbiaocam@nudt.edu.cn
†zzhwcx@163.com
‡phchan@ust.hk

 

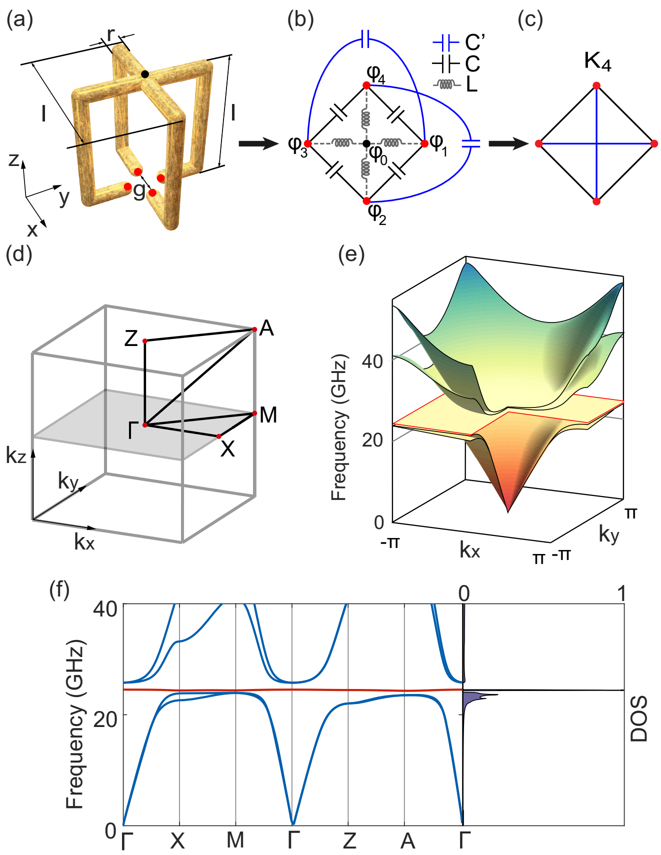


FIG. 1. Schematic view of metallic clawlike structures and flat bands. (a) Geometry of the clawlike metallic structure with $C_4$ rotation symmetry with length $l = 1.95$ mm, gap $g = 0.615$ mm, and diameter $r = 0.21$ mm, as the building block of a simple cubic photonic crystal with lattice constant $a = 3.5$ mm. (b) Effective electric circuit with inductors ($L$) and capacitors ($C$ and $C'$). (c) Complete graph $K_4$ with four vertices and six edges. (d) Three-dimensional first Brillouin zone (FBZ). Black solid lines show the paths followed by energy bands in (f). (e) Isolated flat band (surface with red edge) located in a complete band gap with $k_z = 0$. The fourth quadrant has been cut to show the sectional view for clarity. (f) Photonic band structure along a specific path as indicated in (d), with normalized density of states (DOS) shown in the right panel. The sharp peak in DOS stems from the flat band (red line, left panel) while zero DOS corresponds to the complete band gap.

The computer simulation technology (CST) simulated photonic band structures and density of states (DOS) [48] are shown in Figs. 1(e) and 1(f) with the first Brillouin zone (FBZ) depicted in Fig. 1(d). There is a 3D band gap between the second and fourth bands, inside which lies a third band that is flat throughout the 3D FBZ and has no crossing with other bulk bands. We dubbed it an isolated flat band. The isolated flat band has almost vanishing dispersion among the full 3D FBZ, while the flat bands found in many previous works are typically dispersionless in some particular planes or along some particular directions. As the flat band lies in a gap with the width of 1.73 GHz at around 25 GHz, it cannot hybridize with the dispersive states and spans an orthogonal state space by itself.

We note that most photonic crystals and metamaterials are designed using symmetry as a tool and as such, high degeneracy comes from a combination of the point group of the meta-atom and the space group of the lattice. Here, the high degeneracy arises from finding correspondence to a complete graph. The flat bands arise from local resonances of the metallic claw structure (which carries the spectral characteristics of a complete graph Laplacian matrix) being different from those enabled by a special lattice arrangement (such as the Lieb lattice). The analysis using complete graph theory applies to that of one single meta-atom (an individual metallic claw). When a lattice of metallic claws is used to construct a crystalline lattice arrangement, the collective excitation of the degenerate modes gives rise to the flat bands. From analyzing the complete graph configuration of the metallic claw, we find the relation between number of branches $N_b$ and number of flat bands $N_f$ is $N_f = N_b - 3$.

## III. RELATIONSHIP WITH COMPLETE GRAPH

From a mathematical standpoint, graphs are mathematical structures used to model pairwise relations between objects. The connectivity between the branches in the metallic claw structure can be analyzed by applying graph theory. More specifically, any two branches of the claw structure are coupled electromagnetically together by an effective capacitance as shown in Fig. 1(b). Mathematically speaking, the effective capacitors can be considered as the edges in a graph. Here, we specifically design a structure that has a connectivity that corresponds to the complete graph, where each pair of graph vertices is connected by an edge, as shown in Fig. 1(c) [compared with Fig. 1(b)]. There are six almost equally effective capacitors ($2C' + 4C$) in total between four branches for the $K_4$ case [Figs. 1(a)–1(c)].

Figure 1(c) shows a simple complete graph $K_4$, where each pair of graph vertices (red dots) is connected by an edge (black and blue lines). There are $n$ vertices and $\frac{n(n-1)}{2}$ undirected edges in a complete graph $K_n$. Mathematically, each complete graph $K_n$ is precisely characterized by a Laplacian matrix. For example,

$$L(K_4) = \begin{bmatrix} 3 & -1 & -1 & -1 \\ -1 & 3 & -1 & -1 \\ -1 & -1 & 3 & -1 \\ -1 & -1 & -1 & 3 \end{bmatrix}, \tag{1}$$

where each entry indicates the connection conditions, such as $L_{ii} = 3$ being the degree of vertex $i$ and $L_{ij} = -1$ when $i \neq j$. From a physics viewpoint, each entry of the matrix can also be read as the hopping term in a tight-binding model, such as $L_{ii}$ indicating the on-site energy. Interestingly, the spectra of the Laplacian matrix are given by

$$L_{\rm spec}(K_n) = \Big[0, \underbrace{n, \ldots, n}_{n-1}\Big], \tag{2}$$

which are highly degenerate except for the first 0-eigenvalue state with eigenvector $[1, \ldots, 1]_{1\times n}$. The flat bands of our metacrystal arise from the $n - 1$ nonzero degenerate eigenvalues.

However, this type of pairwise relation is not that easy to realize in practice as each hopping is required to be almost equally valued. In many physical systems in nature, in particular electronic systems, the hopping coefficient typically drops off quickly with distance (such as exponentially). Our work benefits from the special clawlike design, where the gap distance $g$ as shown in Fig. 1(a) can be arbitrarily small theoretically without changing the size of the unit cell. Finally, the capacitors ($C$ and $C'$) approach the same value.

The complete graph configuration can be fully understood through local potential orbitals by analyzing the equivalent electric circuit consisting of capacitors and inductors [Fig. 1(b)]. Following Chua's circuit notation [49,50], the Lagrangian of the circuit reads

$$\begin{aligned}\mathcal{L} = &\frac{C}{2}[(\dot{\varphi}_1-\dot{\varphi}_2)^2+(\dot{\varphi}_2-\dot{\varphi}_3)^2+(\dot{\varphi}_3-\dot{\varphi}_4)^2\\ &+(\dot{\varphi}_4-\dot{\varphi}_1)^2]\\ &+\frac{C'}{2}[(\dot{\varphi}_1-\dot{\varphi}_3)^2+(\dot{\varphi}_2-\dot{\varphi}_4)^2]\\ &-\frac{1}{2L}(\varphi_1^2+\varphi_2^2+\varphi_3^2+\varphi_4^2),\end{aligned} \tag{3}$$

where $\varphi_m$ indicates local potential on the branch $m$ as shown in Fig. 1(b). Without loss of generality, we have assumed $\varphi_0 = 0$. The Euler-Lagrange equation of motion is then

$$I_1 = \frac{d}{dt}\frac{\partial\mathcal{L}}{\partial\dot{\varphi}_1} - \frac{\partial\mathcal{L}}{\partial\varphi_1} = C(2\ddot{\varphi}_1-\ddot{\varphi}_2-\ddot{\varphi}_4)+C'(\ddot{\varphi}_1-\ddot{\varphi}_3)+\frac{1}{L}\varphi_1, \tag{4}$$

where $I_1$ indicating external current has been set to 0 as our system is source free. In the same way, one can obtain $I_{2,3,4} = 0$ and expressing in the matrix form, we get

$$H\Phi = \frac{1}{L\omega^2}\Phi, \tag{5}$$

where $H$ represents the capacitor matrix as

$$H = \begin{bmatrix} 2C+C' & -C & -C' & -C \\ -C & 2C+C' & -C & -C' \\ -C' & -C & 2C+C' & -C \\ -C & -C' & -C & 2C+C' \end{bmatrix}, \tag{6}$$

and $\Phi^T = [\varphi_1, \varphi_2, \varphi_3, \varphi_4]$. The capacitor matrix $H$ shows a strong resemblance to the Laplacian matrix as mentioned above [Eq. (1)]. Different from the ideal complete graph $K_4$, there are two sets of weighted edges $C$ and $C'$ which are slightly different with $C > C'$ ($C'$ has comparably bigger separation).

The condition of $\det(\omega^2 H - \frac{1}{L}I_{4\times 4}) = 0$ gives a nonzero solution to Eq. (5) as

$$\begin{aligned}\omega_3 &= \frac{1}{2\sqrt{CL}},\ \Phi_3^T = \frac{1}{2}[-1, 1, -1, 1]e^{-i\omega t},\\ \omega_4 &= \frac{1}{\sqrt{2(C+C')L}},\ \Phi_4^T = \frac{1}{\sqrt{2}}[0, -1, 0, 1]e^{-i\omega t},\\ \omega_5 &= \frac{1}{\sqrt{2(C+C')L}},\ \Phi_5^T = \frac{1}{\sqrt{2}}[-1, 0, 1, 0]e^{-i\omega t},\end{aligned} \tag{7}$$

where $\Phi_4$ and $\Phi_5$ are degenerate states representing the two orthogonal dipole moments ($p_{x,y}$) of two independent SRRs. In order to be consistent with the band structure simulated

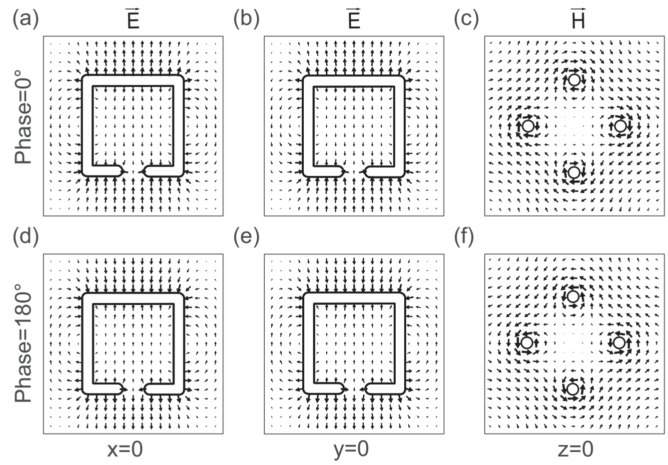


FIG. 2. Electric and magnetic field of the $p_z$ orbital at $\Gamma$ with frequency of 65.48 GHz (the sixth mode).

[Fig. 1(f)], here we start labeling the modes from the third, counting the two bands below the complete band gap. In addition, the eigenmode with four branches oscillating in phase is similar to the $p_z$ orbital excitation with electric and magnetic field as shown in Fig. 2.

Here, the most interesting mode, $\Phi_3$, shows the symmetry of a $d_{x^2-y^2}$ orbital and is orthogonal to the $p_{x,y}$ orbitals ($\Phi_{4,5}$). The flat band of the photonic crystal is the Bloch state comprising this $\Phi_3$ mode. It is easy to find $\omega_3 < \omega_{4,5}$ ($C > C'$), which indicates the flat band locates in the complete band gap. This mode arises only when the two SRRs touch each other. The other four bands (including the first and second, and fourth and fifth bands) can be realized by two separated SRRs following the electromagnetic effective media theory (Fig. 6; see Appendix A) [51,52], where the nonzero bianisotropic term opens the complete band gap. Combining the resonance frequencies from Fig. 1(f) with Eq. (7), one can approximately extract the effective products of $LC$ and $LC'$ [46].

The CST simulated electric and magnetic field distributions of the flat band (the third band) at $\Gamma$ are shown in Fig. 3, which corroborates with our circuit prediction (for other high-symmetry $k$ points see Fig. 4). At $\Gamma$, electromagnetic eigenfields on the cutting plane $z = 0$ oscillate symmetrically.

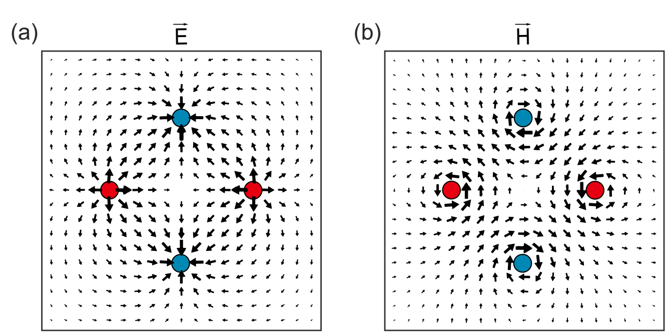


FIG. 3. Eigenfields at $\Gamma$ of the isolated flat band for the $C_4$ metallic claw structure. The direction of the arrow refers to the direction of the electric (magnetic) field while its size represents the local intensity. The eigenfields are in good agreement with our theoretical prediction.

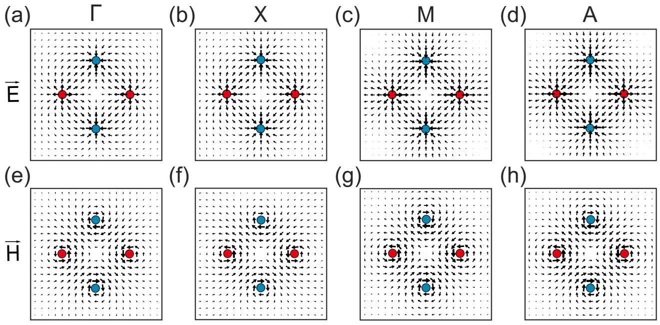


FIG. 4. Eigenfields of the isolated flat band for the $C_4$ metallic claw structure. The direction of the arrow refers to the direction of the electric (magnetic) field while its size represents the local intensity. The eigenfields are in good agreement with our theoretical prediction.

At $X$, $M$, and $A$, the electromagnetic eigenfields remain almost the same, which further indicates the flatness of the isolated band (derived from $\Phi_3$), and the mode profiles are very similar for different momentum $\vec{k}$. The flat band with complete graph configuration is robust. When randomly changing our $K_4$ structure with breaking the $C_4$ rotation symmetry, but preserving the complete graph configuration, the flat band always survives as shown in Fig. 8 (see Appendix C).

Similar to the spectra of a Laplacian matrix [Eq. (2] there are three nonzero eigenvalues in the claw structure shown in Fig. 1(a), two of them being the dipole modes ($p_{x,y}$), leaving one degree of freedom to contribute to the flat band. For claws with more branches, we can predict a general relation between the number of flat bands ($N_f$) and number of branches ($N_b$) as $N_f = N_b - 3$. The dimension of the flat-band subspace gets bigger with an increasing number of branches, squeezing more and more flat bands into a narrow band of frequency.

Schematically, Fig. 7 shows the local orbitals giving rise to the flat bands with number of branches increasing from $N_b = 3$ to 6. Without going through a tedious derivation of the Lagrangian [see Appendix B, Eqs. (B1)–(B4)], all of them can be simply solved using the corresponding Laplacian matrix of a weighted complete graph as shown in the first column, where edges with different colors represent different weights. In realistic metallic claw structures, the different weights correspond to different capacitances between pairs of branches. The level of degeneracy of those flat bands is simply determined by the differences of those capacitances. Although it is hard to make the capacitances exactly the same in practice, a symmetrical design can make the differences smaller. In the second column, we explicitly provide the potential distributions of the dipole excitations where red and light blue indicate, respectively, positive and negative potential distributions with the size representing the amplitude. The blue arrows show the dipole magnitude and directions defined as $\vec{p} = \sum_i r_i\varphi_i$, which are known to be "radiative modes" and heavily dispersive with the momentum $k$. The third column shows higher-multipole excitations. Different from the dipole excitations, the higher-multipole orbitals consist of alternating positive and negative potentials; thus the sum of potential distributions vanishes as $\sum_i r_i\varphi_i = 0$. The modes are effectively "whispering gallery modes" which are known to have very high fidelity, and hence they couple weakly. The dimension of higher-multipole orbitals determines the number of flat bands ($N_f$). For the $K_3$ case, there is no higher-multipole excitation, which agrees well with the geometric prediction of $N_f = N_b - 3$. From $K_4$ on, the number of higher-multipole modes increases linearly with the number of branches as indicated by the orange arrow in Fig. 7.

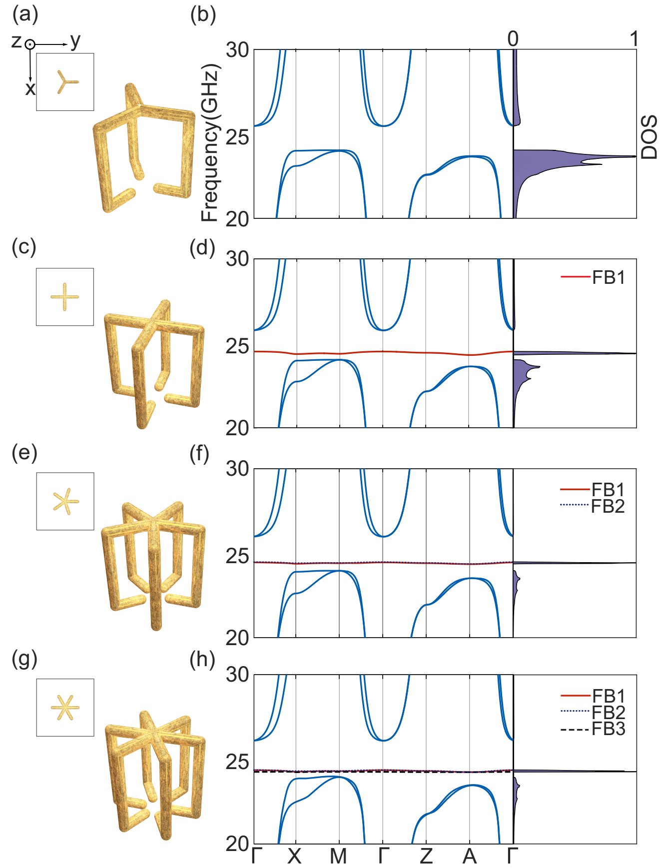


FIG. 5. The relation between number of branches $N_b$ and degeneracy of flat bands (FB) $N_f$. The left column (a,c,e,g) shows metallic claw structures with different $N_b$, with its top view presented in the top left inset. The right column (b,d,f,h) presents the corresponding band structure and DOS from 20 to 30 GHz. When $N_b$ increases, the shape of the dispersive band remains almost unchanged. Furthermore, the flat bands remain at essentially the same frequency as $N_f$ increases, squeezing many bands into a narrow frequency window.

In order to verify those predictions, we show in Fig. 5 the evolution of the band structure as the number of branches changes. In the left inset, we show the metallic claw structures with the number of branches ranging from $N_b = 3$ to 6. These claws are arranged in a simple cubic lattice to build the photonic metacrystal. For simplicity, we also assume all claw structures possess $C_{N_b}$ rotation symmetry in each unit cell, although it is not compatible with the simple cubic Bravais lattice when $N_b \neq 4$. The orientation of the claw structure within the unit cell does not affect the existence of the flat bands. In the right column, the corresponding band structures and DOS [48] for different $N_b$ are shown. We have normalized the DOS [48] within the interval of 01 to reveal the contrast between the flat bands and dipolar pass bands. In order to clearly count the number of isolated flat bands and to check more details, different line styles are used and indicated in the figure. We find that the bands will become flatter when each unit cell gets bigger (keeping the size of the claw structure the same). Therefore, the small dispersions of the flat bands originate from the weak coupling of the localized modes between neighboring meta-atoms. However, when the lattice constant gets too big, the gap will close as the Bragg scattering of the dipolar modes becomes too weak to sustain a complete gap. In that limit, the flat bands will intersect with the dipolar band manifold and no longer exist in a clean absolute gap.

As predicted above, we observe a $N_f = N_b - 3$ rule for the claw structures. When $N_b = 3$, there is no flat band even though the band-gap width is larger than 1.4 GHz [52]. The DOS peak at the frequency corresponds to the lower boundary of the band gap. Isolated flat bands emerge when $N_b > 3$, and all are confined inside a narrow frequency window (from 24.24 to 24.53 GHz for the structural parameters specified in Fig. 1). The number of flat bands inside the band gap increases with the number of branches in the claw, and the corresponding DOS in the flat-band frequency window grows dramatically, which can potentially facilitate applications that require a high photonic DOS. The $K_{20}$ case is shown in Figs. 9(a) and 9(b) (see Appendix D) to further illustrate this phenomenon. In particular, there are 17 flat bands in total as one can check in Fig. 9(c), confirming again the $N_f = N_b - 3$ rule.

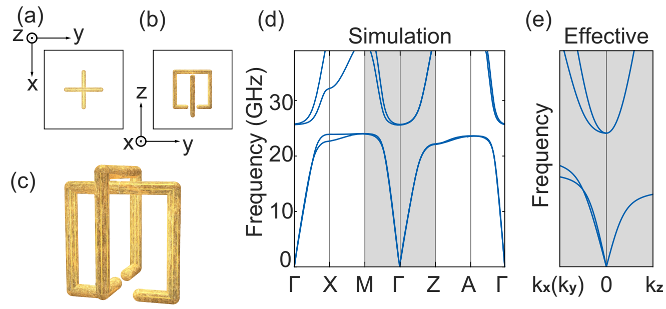


FIG. 6. Two separated SRRs and corresponding band structure with a complete band gap. (a–c) Geometry of two separated SRRs. (d) shows the simulated band structure; (e) shows the band structure from effective media theory. The shadow regions give the qualitative comparison.

## IV. DISCUSSION

A unique feature of the metallic claw design, as the realization of a complete graph, is that the dimension of the flat-band set depends on the number of branches and as such, we can arbitrarily enlarge the flat-band subspace without shifting their operating frequency. As the spectral property of a complete graph is mainly determined by geometry and connectivity, the structural details of the meta-atoms are unimportant, and hence the flat bands and the related phenomena are robust even if the real samples deviate from the theoretical design (Fig. 10; see Appendix E). On the other hand, their very high DOS and the high-$Q$ factors of the high-order orbitals render these complete-graph-inspired systems sensitive to environmental external fields, making them good platforms for information sensing. In addition, the local resonances arising from the complete graph configuration behave similarly to conventional spherical orbitals ($s$, $p$, $d$, $f$, etc.); for example the number of degenerate modes increases with the number of branches (angular momentum for spherical orbitals). However, there are some counterintuitive differences, which include the resonances being protected by an underlying connectivity relationship (rather than rotation symmetries) and different higher multiples share the same resonance frequency. To some extent, we propose another mechanism of local orbitals with graph theory.

## V. CONCLUSION

In conclusion, we have designed clawlike metallic meta-atoms inspired by complete graph theory. We investigated photonic crystals composed of these meta-atoms and found isolated flat bands confined in a narrow frequency window. Different from previous works based on lattice geometry, the flat-band mode is insensitive to structural and lattice parameter perturbations. We found a simple relation governing the number of flat bands ($N_f$), which can easily be understood by mapping to the corresponding weighted complete graph. The highly degenerate flat bands and the associated high DOS persist even if the lattice (translation symmetry) is destroyed as the phenomena originate from internal degrees of freedom of the metallic claws.

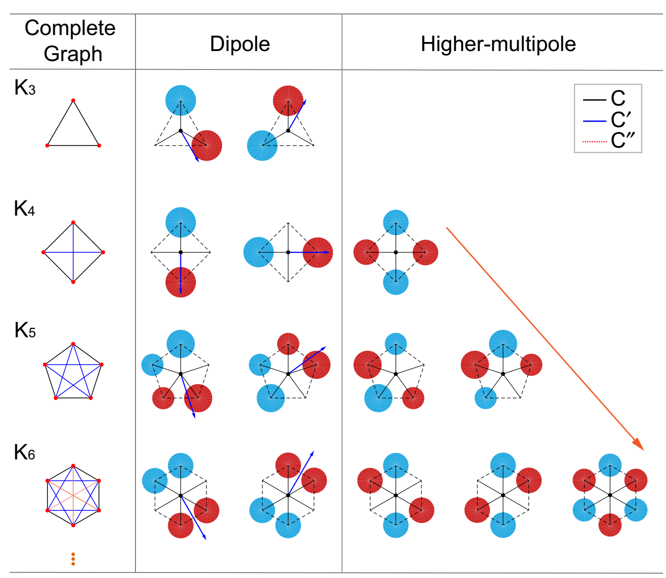


FIG. 7. Complete graph analogy of the metallic clawlike structures. The left column illustrates equivalent complete graph circuits of different $N_b$ (the number of branches for each "claw"), while the middle and the right columns show their corresponding eigenpotential distributions. Red (light blue) disk represents positive (negative) electric potential, and its radius represents the absolute value of each potential. The number of eigenstates increases with $N_b$. For each single clawlike metallic structure, there are two noncollinear dipole excitations. Higher-multipole excitations appear when $N_b \geqslant 4$, concomitant with the emergence of flat bands. The number of flat bands ($N_f$) varies with $N_b$ as $N_f = N_b - 3$.

### ACKNOWLEDGMENTS

This work is supported by the National Natural Science Foundation of China (Grant No. 11674396). The work in Hong Kong is supported by the Research Grants Council of Hong Kong (Grants No. AoE/P-02/12 and No. C6013-18G).

H.W. and B.Y. contributed equally to this work.


### APPENDIX A: ELECTROMAGNETIC EFFECTIVE MEDIA ANALYSIS

As shown in Figs. 6(a)–6(c), we consider two separated SRRs. For brevity, we neglect the Ohmic loss and the intra- and interlayer interactions. The corresponding constitutive matrices of omega-type bianisotropic metamaterials are [51]

$$D = \overleftrightarrow{\varepsilon}E + i\overleftrightarrow{\gamma}H$$
$$B = \overleftrightarrow{\mu}H - i\overleftrightarrow{\gamma}^t E, \tag{A1}$$

where $\overleftrightarrow{\varepsilon}$, $\overleftrightarrow{\mu}$, and $\overleftrightarrow{\gamma}$ are the permittivity, permeability, and magnetoelectric tensors, respectively. Their explicit forms are

$$\overleftrightarrow{\varepsilon}= \begin{bmatrix} \varepsilon & 0 & 0 \\ 0 & \varepsilon & 0 \\ 0 & 0 & 1 \end{bmatrix}, \ \overleftrightarrow{\mu}= \begin{bmatrix} \mu & 0 & 0 \\ 0 & \mu & 0 \\ 0 & 0 & 1 \end{bmatrix}, \ \overleftrightarrow{\gamma} = \begin{bmatrix} 0 & \gamma & 0 \\ -\gamma & 0 & 0 \\ 0 & 0 & 0 \end{bmatrix}, \tag{A2}$$

and

$$\varepsilon = 1+ \frac{l^2}{L}\frac{1}{\omega_0^2-\omega^2}, \ \mu = 1+ \frac{A^2}{L}\frac{\omega^2}{\omega_0^2-\omega^2}, \ \gamma = \frac{lA}{L}\frac{\omega}{\omega_0^2-\omega^2}, \tag{A3}$$

where $l$ and $A$ indicate effective length and area of SRR; $\omega_0 = 1/\sqrt{LC}$ indicates the resonance frequency of SRR with $L/C$ being the effective inductance/capacitance. We have set light velocity $c = 1$ during the derivation.

The bianisotropic term $\gamma$ opens the complete band gap as shown in Fig. 6(d) [52]. The band structure plotted with effective parameters $l = 1$, $A = 1$, $L = 2$, and $\omega_0 = 1$ is shown in Fig. 6(e), which qualitatively shows similar features to Fig. 6(d).

Obviously, one cannot expect the flat band (resonance mode) from the lattice of two separated SRRs. However, it supports the complete band gap due to the nonzero bianisotropic term [52].

### APPENDIX B: EQUIVALENT ELECTRIC CIRCUIT MODEL

Using similar derivation techniques as shown in Eqs. (3)–(6) in the main text, the dynamic matrices for $K_3 - K_6$ are explicitly given as (with notations consistent with Fig. 7)

$$H_3 = \begin{bmatrix} 2C & -C & -C \\ -C & 2C & -C \\ -C & -C & 2C \end{bmatrix}, \tag{B1}$$

$$H_4 = \begin{bmatrix} 2C+C' & -C & -C' & -C \\ -C & 2C+C' & -C & -C' \\ -C' & -C & 2C+C' & -C \\ -C & -C' & -C & 2C+C' \end{bmatrix}, \tag{B2}$$

$$H_5 = \begin{bmatrix} 2C+2C' & -C & -C' & -C' & -C \\ -C & 2C+2C' & -C & -C' & -C' \\ -C' & -C & 2C+2C' & -C & -C' \\ -C' & -C' & -C & 2C+2C' & -C \\ -C & -C' & -C' & -C & 2C+2C' \end{bmatrix}, \tag{B3}$$

and

$$H_6 = \begin{bmatrix} C_0 & -C & -C' & -C'' & -C' & -C \\ -C & C_0 & -C & -C' & -C'' & -C' \\ -C' & -C & C_0 & -C & -C' & -C'' \\ -C'' & -C' & -C & C_0 & -C & -C' \\ -C' & -C'' & -C' & -C & C_0 & -C \\ -C & -C' & -C'' & -C' & -C & C_0 \end{bmatrix}, \tag{B4}$$

with $C_0 = 2C + 2C' + C''$.

### APPENDIX C: ROBUSTNESS OF FLAT BAND WITH COMPLETE GRAPH CONFIGURATION

We randomly change our $K_4$ structure with breaking the $C_4$ rotation symmetry, but preserving the complete graph configuration to test the robustness of flat bands. We use four different random ranges as [–10°, +10°], [–20°, +20°], [–30°, +30°] and [–40°, +40°]. Each range randomly outputs four rotation angles. We then impose the four angles upon each original $K_4$ branch [Fig. 8(a)] in order. The results are shown in Fig. 8, where the flat bands remain almost unchanged. One can claim it is the underlying connectivity nature of metallic claw structure that enables the flat bands, namely, a complete graph configuration. We even consider an extreme case, as shown in Figs. 8(k) and 8(l), where one still can see a flat band. Certainly, with imposing high symmetry onto the claw structure, the flat band will have some nice features, such as locating in a wider complete band gap.

### APPENDIX D: FLAT BANDS FOR METALLIC CLAWS WITH MANY BRANCHES: THE $K_{20}$ CASE

We calculate the band structure for the case where there are 20 branches for a metallic claw, as shown in Figs. 9(a) and 9(b). Figure 9(c) shows the set of degenerate isolated

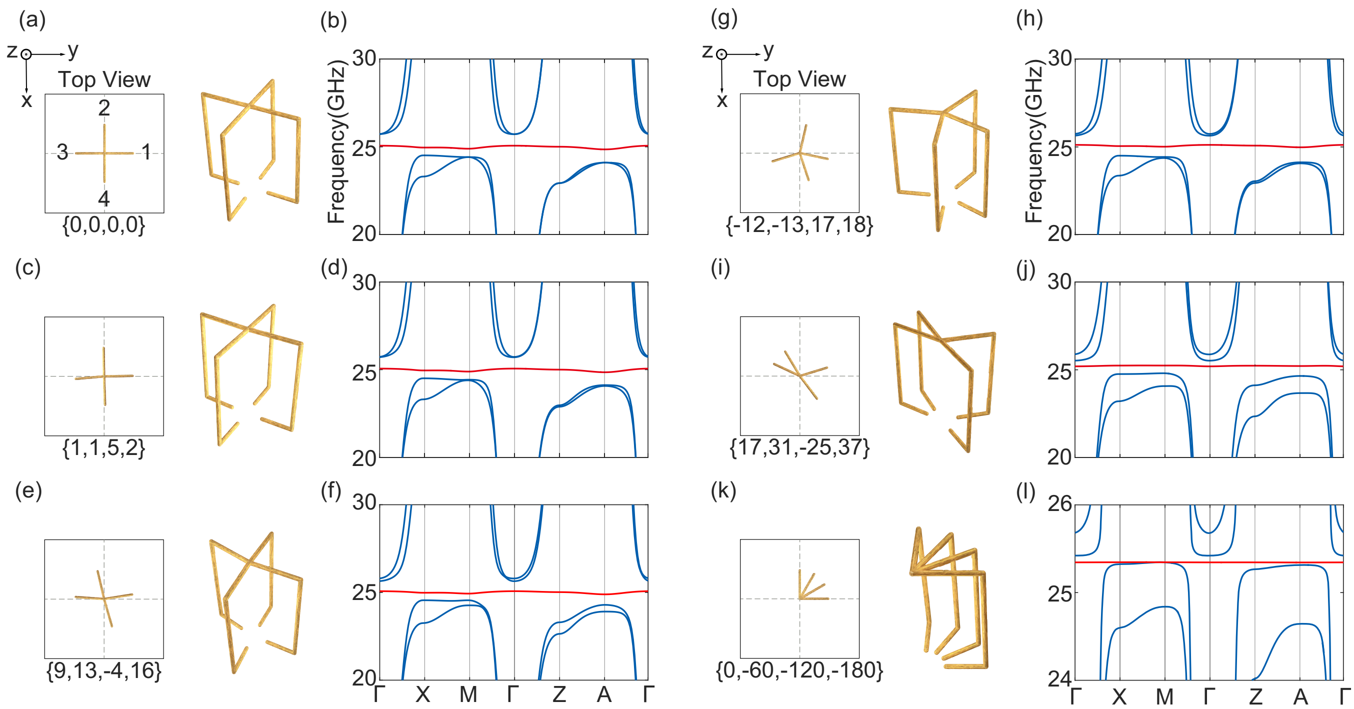


FIG. 8. Band structure with randomly changing the branch orientation for the $K_4$ case. (c,d), (e,f), (g,h), (i,j) correspond to four random ranges [–10°, 10°], [–20°, 20°], [–30°, 30°] and [–40°, 40°], respectively. Each random range outputs four random rotation angles as indicated in the braces in each top-view inset. The four random rotation angles are imposed onto each branch in order as defined in panel (a), where the negative (positive) sign indicates clockwise (anticlockwise) rotation based on the original orientation (a). (k,l) shows an extreme case with rotation angles indicated.

flat bands locating in the band gap ranges from 25.1 to 25.8 GHz. In contrast with those dispersive dipolar bands, these flat bands give rise to very high DOS as these bands are squeezed into a narrow bandwidth. According to the geometric principle, we predict that there should be $N_f = N_b - 3 = 17$ isolated flat bands in the band gap, which has been confirmed by zooming in the view to 25.1–25.8 GHz [Fig. 9(c)].

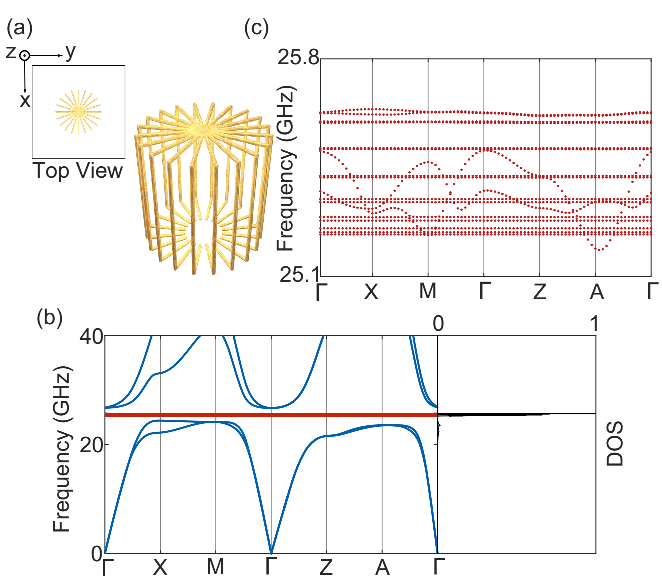


FIG. 9. $K_{20}$ metallic claw provides 17 isolated flat bands. (a) Metallic claw structure when $N_b = 20$. (b) Set of isolated flat bands and the corresponding high density of states (DOS). (c) There are 17 flat bands in total within the range from 25.1 to 25.8 GHz.

## APPENDIX E: ROBUSTNESS AGAINST VARIOUS PERTURBATIONS

One of the distinctive features of the metallic claw structure is the stability under variation of structural details. As demonstrated in Fig. 10(a), there is an isolated flat band in the band gap between the second band and the fourth band when the length of cross section $r$ reduces from 0.21 to 0.18 mm. The band structures of $r = 0.18$ mm are basically identical with those of $r = 0.21$ mm. Figure 10(b) shows the situation when the lattice constant increases from

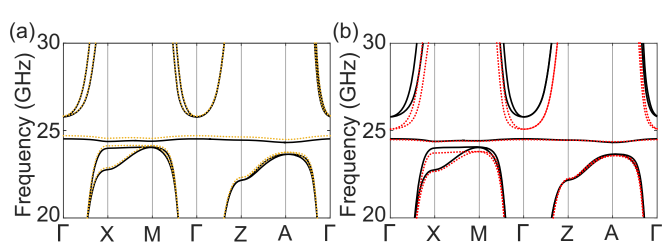


FIG. 10. Contrast of band structure under lattice distortions. (a) $r = 0.18$ mm (yellow dashed lines) and $r = 0.21$ mm (black solid lines). (b) $a = 4$ mm (red dashed line) and $a = 3.5$ mm (black solid lines).

3.5 to 4 mm, which is also quite a big change for the lattice (keeping the size of the metallic structure the same). The trend of the band structure is unaltered, as the distance between branches in adjacent unit cells is increased, resulting in weaker coupling between adjacent unit cells, and isolated flat bands remain essentially unchanged. This is because the flat bands arise from the local resonance of the metallic claw structure.


[1] B. Sutherland, Localization of electronic wave functions due to local topology, Phys. Rev. B **34**, 5208 (1986).

[2] M. Arai, T. Tokihiro, T. Fujiwara, and M. Kohmoto, Strictly localized states on a two-dimensional Penrose lattice, Phys. Rev. B **38**, 1621 (1988).

[3] E. H. Lieb, Two Theorems on the Hubbard Model, Phys. Rev. Lett. **62**, 1201 (1989).

[4] A. Ramachandran, A. Andreanov, and S. Flach, Chiral flat bands: Existence, engineering, and stability, Phys. Rev. B **96**, 161104 (2017).

[5] D. Leykam, A. Andreanov, and S. Flach, Artificial flat band systems: From lattice models to experiments, Adv. Phys.: X **3**, 1473052 (2018).

[6] D. Leykam and S. Flach, Perspective: Photonic flatbands, APL Photonics **3**, 070901 (2018).

[7] T. Baba, Slow light in photonic crystals, Nat. Photonics **2**, 465 (2008).

[8] J. Li, T. P. White, L. O'Faolain, A. Gomez-Iglesias, and T. F. Krauss, Systematic design of flat band slow light in photonic crystal waveguides, Opt. Express **16**, 6227 (2008).

[9] S. A. Schulz, J. Upham, L. O'Faolain, and R. W. Boyd, Photonic crystal slow light waveguides in a kagome lattice, Opt. Lett. **42**, 3243 (2017).

[10] S. Mukherjee, A. Spracklen, D. Choudhury, N. Goldman, P. Öhberg, E. Andersson, and R. R. Thomson, Observation of a Localized Flat-Band State in a Photonic Lieb Lattice, Phys. Rev. Lett. **114**, 245504 (2015).

[11] W. Maimaiti, S. Flach, and A. Andreanov, Universal $d = 1$ flat band generator from compact localized states, Phys. Rev. B **99**, 125129 (2019).

[12] R. W. Boyd, Material slow light and structural slow light: Similarities and differences for nonlinear optics [Invited], J. Opt. Soc. Am. B **28**, A38 (2011).

[13] Z. Chen, M. Segev, and D. N. Christodoulides, Optical spatial solitons: Historical overview and recent advances, Rep. Prog. Phys. **75**, 086401 (2012).

[14] L. Santos, M. A. Baranov, J. I. Cirac, H.-U. Everts, H. Fehrmann, and M. Lewenstein, Atomic Quantum Gases in Kagomé Lattices, Phys. Rev. Lett. **93**, 030601 (2004).

[15] A. Mielke, Exact ground states for the Hubbard model on the kagome lattice, J. Phys. A: Math. Gen. **25**, 4335 (1992).

[16] H. Tasaki, Ferromagnetism in the Hubbard Models with Degenerate Single-Electron Ground States, Phys. Rev. Lett. **69**, 1608 (1992).

[17] H. Tasaki, Hubbard model and the origin of ferromagnetism, Eur. Phys. J. B **64**, 365 (2008).

[18] A. Szameit and S. Nolte, Discrete optics in femtosecond-laser-written photonic structures, J. Phys. B: At., Mol. Opt. Phys. **43**, 163001 (2010).

[19] A. Crespi, G. Corrielli, G. D. Valle, R. Osellame, and S. Longhi, Dynamic band collapse in photonic graphene, New J. Phys. **15**, 013012 (2013).

[20] D. Guzmán-Silva *et al.*, Experimental observation of bulk and edge transport in photonic Lieb lattices, New J. Phys. **16**, 063061 (2014).

[21] R. A. Vicencio, C. Cantillano, L. Morales-Inostroza, B. Real, C. Mejía-Cortés, S. Weimann, A. Szameit, and M. I. Molina, Observation of Localized States in Lieb Photonic Lattices, Phys. Rev. Lett. **114**, 245503 (2015).

[22] S. Xia *et al.*, Demonstration of flat-band image transmission in optically induced Lieb photonic lattices, Opt. Lett. **41**, 1435 (2016).

[23] S. Endo, T. Oka, and H. Aoki, Tight-binding photonic bands in metallophotonic waveguide networks and flat bands in kagome lattices, Phys. Rev. B **81**, 113104 (2010).

[24] F. Morichetti, C. Ferrari, A. Canciamilla, and A. Melloni, The first decade of coupled resonator optical waveguides: bringing slow light to applications, Laser Photonics Rev. **6**, 74 (2012).

[25] Y. Nakata, T. Okada, T. Nakanishi, and M. Kitano, Observation of flat band for terahertz spoof plasmons in a metallic kagome lattice, Phys. Rev. B **85**, 205128 (2012).

[26] M. Hafezi, S. Mittal, J. Fan, A. Migdall, and J. M. Taylor, Imaging topological edge states in silicon photonics, Nat. Photonics **7**, 1001 (2013).

[27] T. Jacqmin, I. Carusotto, I. Sagnes, M. Abbarchi, D. D Solnyshkov, G. Malpuech, E. Galopin, A. Lemaître, J. Bloch, and A. Amo, Direct Observation of Dirac Cones and a Flatband in a Honeycomb Lattice for Polaritons, Phys. Rev. Lett. **112**, 116402 (2014).

[28] F. Baboux, L. Ge, T. Jacqmin, M. Biondi, E. Galopin, A. Lemaître, L. Le Gratiet, I. Sagnes, S. Schmidt, H. E. Türeci, A. Amo, and J. Bloch, Bosonic Condensation and Disorder-Induced Localization in a Flat Band, Phys. Rev. Lett. **116**, 066402 (2016).

[29] Y. Nakata, Y. Urade, T. Nakanishi, F. Miyamaru, M. Wada Takeda, and M. Kitano, Supersymmetric correspondence in spectra on a graph and its line graph: From circuit theory to spoof plasmons on metallic lattices, Phys. Rev. A **93**, 043853 (2016).

[30] S. Kajiwara, Y. Urade, Y. Nakata, T. Nakanishi, and M. Kitano, Observation of a nonradiative flat band for spoof surface plasmons in a metallic Lieb lattice, Phys. Rev. B **93**, 075126 (2016).

[31] S. Klembt *et al.*, Polariton condensation in S- and P-flatbands in a two-dimensional Lieb lattice, Appl. Phys. Lett. **111**, 231102 (2017).

[32] X.-Y. Zhu *et al.*, $Z_2$ topological edge state in honeycomb lattice of coupled resonant optical waveguides with a flat band, Opt. Express **26**, 24307 (2018).

[33] H. Takeda, T. Takashima, and K. Yoshino, Flat photonic bands in two-dimensional photonic crystals with kagome lattices, J. Phys.: Condens. Matter **16**, 6317 (2004).

[34] C. Xu *et al.*, Design of full-$k$-space flat bands in photonic crystals beyond the tight-binding picture, Sci. Rep. **5**, 18181 (2015).

[35] N. Myoung, H. C. Park, A. Ramachandran, E. Lidorikis, and J.-W. Ryu, Flat-band localization and self-collimation of light in photonic crystals, Sci. Rep. **9**, 2862 (2019).
[36] D. L. Bergman, C. Wu, and L. Balents, Band touching from real-space topology in frustrated hopping models, Phys. Rev. B **78**, 125104 (2008).
[37] S. Flach, D. Leykam, J. D. Bodyfelt, P. Matthies, and A. S. Desyatnikov, Detangling flat bands into Fano lattices, EPL **105**, 30001 (2014).
[38] C. Weeks and M. Franz, Flat bands with nontrivial topology in three dimensions, Phys. Rev. B **85**, 041104 (2012).
[39] D. Green, L. Santos, and C. Chamon, Isolated flat bands and spin-1 conical bands in two-dimensional lattices, Phys. Rev. B **82**, 075104 (2010).
[40] G. Tarnopolsky, A. J. Kruchkov, and A. Vishwanath, Origin of Magic Angles in Twisted Bilayer Graphene, Phys. Rev. Lett. **122**, 106405 (2019).
[41] T. Ozawa *et al.*, Topological photonics, Rev. Mod. Phys. **91**, 015006 (2019).
[42] F. D. M. Haldane and S. Raghu, Possible Realization of Directional Optical Waveguides in Photonic Crystals with Broken Time-Reversal Symmetry, Phys. Rev. Lett. **100**, 013904 (2008).
[43] S. Raghu and F. D. M. Haldane, Analogs of quantum-Hall-effect edge states in photonic crystals, Phys. Rev. A **78**, 033834 (2008).
[44] L. Lu, J. D. Joannopoulos, and M. Soljačić, Topological photonics, Nat. Photonics **8**, 821 (2014).
[45] J. A. Bondy and U. S. R. Murty, *Graph Theory with Applications* (Macmillan, London, 1976).
[46] C. Caloz and T. Itoh, *Electromagnetic Metamaterials: Transmission Line Theory and Microwave Applications* (John Wiley & Sons, Inc., Hoboken, NJ, 2005).
[47] R. Zhao, T. Koschny, and C. M. Soukoulis, Chiral metamaterials: Retrieval of the effective parameters with and without substrate, Opt. Express **18**, 14553 (2010).
[48] B. Liu, S. G. Johnson, J. D. Joannopoulos, and L. Lu, Generalized Gilat–Raubenheimer method for density-of-states calculation in photonic crystals, J. Opt. **20**, 044005 (2018).
[49] O. Feely, in *Chaos, CNN, Memristors and Beyond*, edited by A. Adamatzky and G. Chen (World Scientific, Singapore, 2012), pp. 36–40.
[50] E. Zhao, Topological circuits of inductors and capacitors, Ann. Phys. **399**, 289 (2018).
[51] B. Yang *et al.*, Ideal Weyl points and helicoid surface states in artificial photonic crystal structures, Science **359**, 1013 (2018).
[52] Y. Yang *et al.*, Realization of a three-dimensional photonic topological insulator, Nature **565**, 622 (2019).